Case Studies in Construction Materials 21 (2024) e04008

Contents lists available at ScienceDirect

Case Studies in Construction Materials

journal homepage: www.elsevier.com/locate/cscm

Case study

New Zealand pumicite as a precursor in producing alkaline cement with aluminate-based activators

Roohollah Kalatehjari [a,*], Elmira Khaksar Najafi [b], Afshin Asadi [c], Martin Brook [d]

[a] Built Environment Engineering Department, School of Future Environments, Auckland University of Technology, Auckland 1010, New Zealand
[b] James Watt School of Engineering, University of Glasgow, United Kingdom
[c] Wilton Joubert Consulting Engineers, Auckland, New Zealand; EnvoGeotechnique Ltd., Auckland, New Zealand
[d] School of Environment, University of Auckland, Auckland 1010, New Zealand

ARTICLE INFO

Keywords:
New Zealand Pumicite
Pumice
Alkali-Activated Cement
Sodium Aluminate
Microstructural Characterisation

ABSTRACT

This study investigates the activation of New Zealand pumicite (pumice powder) using sodium aluminate ($NaAlO_2$) solution, both alone and in combination with 10 M KOH solution, at various weight ratios of 1, 3, and 5, to produce alkali-activated cement. Compressive strength tests and microstructural analyses were conducted to assess the effects of activator/precursor ratios, activator type, aging time, and curing temperature (65°C for 72 hours or room temperature). The internal porosity of the pumicite played a key role in aluminosilicate phase dissolution and mobility, resulting in similar compressive strengths across different ratios. $NaAlO_2$ alone achieved compressive strengths of 60 MPa and 67 MPa after 4 and 65 days, respectively, while the binary solutions showed reduced strength with increased aging. Room temperature curing required almost three times the aging period to match the 28-day compressive strengths achieved after curing at 65°C for 72 hours. Microstructural analyses revealed that $NaAlO_2$ solution adjusted the Si/Al ratio, forming high-Al and high-Si gels as well as zeolite-A, underscoring its benefits. This study demonstrates the potential of using locally sourced New Zealand pumicite as a precursor in alkali-activated cement, particularly in regions lacking traditional industrial by-products.

1. Introduction

In an era of growing environmental concerns, sustainability has become a crucial consideration across all industries, including construction. The annual production of cement is approximately 4 billion tonnes, while concrete production is estimated at around 10.5 billion tonnes [1]. Cement, a vital component of concrete, is associated with a significant carbon footprint, largely due to the high energy consumption from fossil fuels, contributing roughly 8 % of global CO_2 emissions [2]. This impact is primarily driven by the thermal decomposition of calcium carbonate to produce Portland Cement (PC), which exacerbates global warming and poses a threat to the environment. To meet the net-zero objectives of the Paris Agreement [3]. It is critical to explore and implement alternative binders with a lower environmental impact than PC, thus reducing the construction industry's carbon footprint. Alkali-activated materials (AAMs) have been proven effective in reducing energy consumption by up to 50 % and CO_2 emissions by up to 80 % compared to Portland cement production [4–6]. It is widely recognised that approximately 90 % of the environmental footprint of

* Correspondence to: Auckland University of Technology, WZ Building, 6 St Paul Street, Auckland 1010, New Zealand.
E-mail addresses: r.kalatehjari@aut.ac.nz (R. Kalatehjari), Elmira.KhaksarNajafi@glasgow.ac.uk (E. Khaksar Najafi), afshin@envo-geotechnique.co.nz (A. Asadi), m.brook@auckland.ac.nz (M. Brook).

https://doi.org/10.1016/j.cscm.2024.e04008
Received 13 August 2024; Received in revised form 17 November 2024; Accepted 18 November 2024
Available online 20 November 2024

alkali-activated binders originates from the activator. Nevertheless, alkali-activated cements can still achieve a 40–80 % reduction in CO_2 emissions compared to Portland cement as Portland cement production requires significantly higher temperatures than alkali activators [7].

Decades of research into alkali-activated binders highlight their immense potential as the next generation of construction materials [8]. AAMs are formed under highly alkaline conditions, where dissolved $[SiO_4]^{4-}$ and $[AlO_4]^{5-}$ tetrahedral units (gels) released from reactive aluminosilicates (precursors) bond by sharing oxygen atoms to form amorphous aluminosilicate chains and ring polymers with Si^{4+} and Al^{3+} units [9,10]. The chemical composition and structure of the precursors determine their reactivity, influencing the type of gel formed, secondary reactions, and the strength development in alkaline cements [11,12].

There have been limited attempts to use pumicite (pumice powder) with amorphous industrial by-products for alkaline cement production [13–24]. Pumicite is a fine-grained, powdered, or dust form of pumice, a type of volcanic glass, primarily composed of amorphous aluminosilicates, making it a potential precursor for alkaline activation. This low-density, silica-rich, and porous volcanic material forms during phases of violent and gaseous volcanic activity [25,26]. Due to rapid cooling, the atoms do not form crystalline structures, resulting in an amorphous composition. Pumicite deposits in New Zealand (NZ) are found in several areas of the central North Island, originating from a series of rhyolitic volcanic eruptions centred in the Taupo and Rotorua regions within the Taupo Volcanic Zone (TVZ) [27,28]. The approximate distribution of these deposits is shown in Fig. 1 [27].

Previous studies indicate a deficiency of alumina units compared to silica units in pumicite, resulting in an initial SiO_2/Al_2O_3 ratio of 4 (Si/Al = 2), which is considered optimal for the mechanical strength of alkali-activated cement [29–31]. In fact, an excess of silica reduces compressive strength, as aluminium is essential for bonding silicon tetrahedra [32], and its insufficiency hampers condensation reactions, preventing the sufficient formation of geopolymeric gels due to unreacted silicon [29,31]. This highlights the need for incorporating pumicite in binary or ternary blends with materials containing amorphous phases of calcium [33,34] or aluminium [21,35]. In such blends, Ca or Al can aid in the formation of geopolymeric gels, such as C-A-S-H (Calcium-Aluminium-Silicate-Hydrate) and N-A-S-H (Sodium-Aluminium-Silicate-Hydrate) gels.

Despite the recognised potential of pumice as an abundant volcanic rock for use in alkali-activated materials, the application of New Zealand pumicite as a precursor has yet to be explored. Furthermore, previous studies have not investigated the use of soluble aluminate to modify the reactive SiO_2/Al_2O_3 ratio of pumicite, where pumicite could act as the sole precursor in the production of alkali-activated cement. Therefore, this study aims to evaluate the effectiveness of aluminate-based reactions in promoting the alkali activation of New Zealand pumicite. In doing so, this study not only seeks to activate NZ pumicite but also addresses the need to reduce

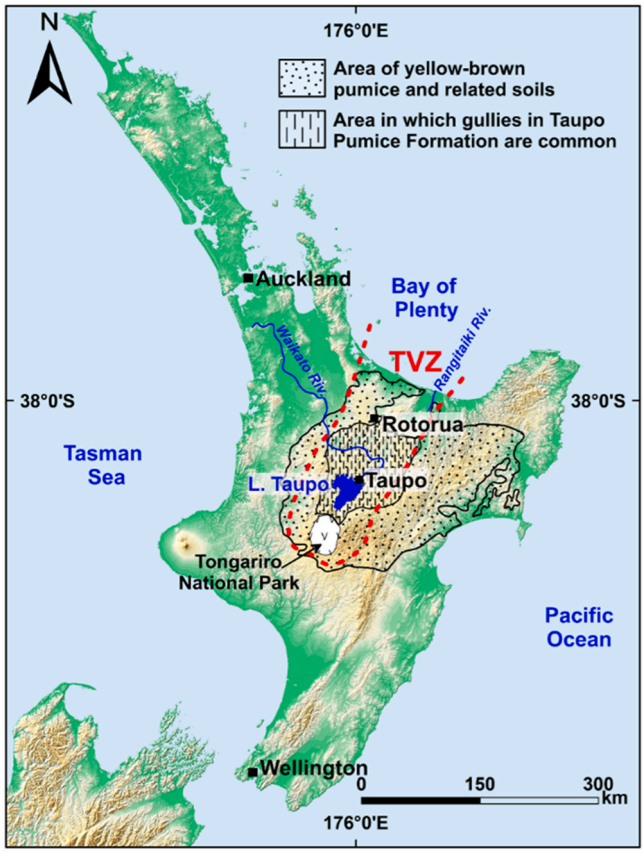

Fig. 1. Common areas where pumicite is found in the central North Island, New Zealand (based on Selby and Hosking [27]).

reliance on supplementary materials, which may contain trace amounts of heavy metals and pose long-term risks to natural resources [36].

In this context, the microstructural, chemical, and mineralogical characteristics of New Zealand pumicite were evaluated to determine its suitability for alkali activation. The study begins by characterising a commercially available pumicite, with a focus on optimising its specific surface area through various grinding regimes, informed by successful precedents in the literature [13–24].

Using a unique chemical composition, the research further investigates different mixtures of potassium hydroxide and sodium aluminate to understand how soluble aluminate enhances the alkali activation potential of NZ pumicite. The effects of key variables, such as the activator/precursor ratio, curing time, and temperature, on the properties of the resulting alkali-activated cement are thoroughly examined and discussed. Techniques such as Unconfined Compressive Strength (UCS) tests, Scanning Electron Microscopy (SEM) coupled with Energy Dispersive Spectroscopy (EDS), X-ray Diffraction (XRD), and Fourier Transform Infrared Spectroscopy (FTIR) will be employed to comprehensively analyse the activation process and its outcomes.

2. Materials and methods

2.1. Materials

2.1.1. Pumicite precursor

The pumicite used in the study was supplied by Pure Ingredients Company, New Zealand (reference code: EF100037(PUMICE-MILL02). The pH of the pumicite was reported to vary from 6.5 to 8.0. Particle size distribution of the unground pumicite (Fig. 2a, b) was obtained from Laser Particle Size Distribution (LPSD) using a Mastersizer 2000 Analyzer according to ASTM-E3340−22 [37].

The external specific surface area (SSA) and Brunauer, Emmett, and Teller (BET) surface area of the unground pumicite, obtained from LPSD and BET analyses, are 0.93 m^2/g and 10.86 m^2/g, respectively. BET analysis was conducted using nitrogen gas adsorption-desorption isotherms at liquid nitrogen temperature (−196°C). The significant difference between these two values is attributed to the internal porosity of the pumicite, as illustrated in the SEM image (Fig. 3).

X-ray Diffraction (XRD) and X-ray Fluorescence (XRF) analyses were conducted to evaluate the mineralogy, amorphous content, and chemical composition of the pumicite, with results presented in Fig. 4 and Table 1, respectively. The XRD pattern revealed the presence of 29.18 % aluminosilicate crystalline phases, including albite ($NaAlSi_3O_8$), paragonite ($NaAl_2(Si_3Al)O_{10}(OH)_2$), and silicon dioxide ($SiO_2$), indicating a remaining 70.82 % amorphous phase. The XRF results showed a SiO_2/Al_2O_3 ratio of 5.28, which exceeds the optimal ratio of 4, suggesting sub-optimal aluminium content in New Zealand pumicite for alkali activation [38]. The Loss on Ignition (LOI) was determined to be 2.5–3.2 % by weight of the sample, following the method outlined in ASTM-C114−18 [39]. The calcium and magnesium contents of the pumicite were also considered insufficient to effectively contribute to the activation process.

2.1.2. Alkaline activators

Four different aluminate-based activators were used for sample fabrication, including a $NaAlO_2$ solution designated as K0, and three binary solutions prepared by combining KOH and $NaAlO_2$ in weight ratios of 1, 3, and 5, designated as K1, K3, and K5, respectively. The inclusion of sodium aluminate in this study is based on preliminary XRF test results, which suggest a lower-than-optimal SiO_2/Al_2O_3 ratio for alkali activation [38]. The binary solutions consisted of a mixture of 10 M KOH solution and $NaAlO_2$ solution at weight ratios of 1, 3, and 5. $NaAlO_2$ 50 %, containing 50–60 % Al_2O_3 and 37–45 % Na_2O, was supplied by Sigma-Aldrich, New Zealand, with an Al_2O_3/Na_2O molar ratio of approximately 1.34.

KOH pellets (88 wt% purity), with a specific gravity of 2.04 at 20°C, were supplied by ThermoFisher. The 10 M KOH solution was prepared by dissolving the KOH pellets in distilled water, mixed in a container on ice until fully dissolved, and then left to cool at room temperature for 24 hours. KOH was the only hydroxide solution used in this study, with a proven track record in pumice activation

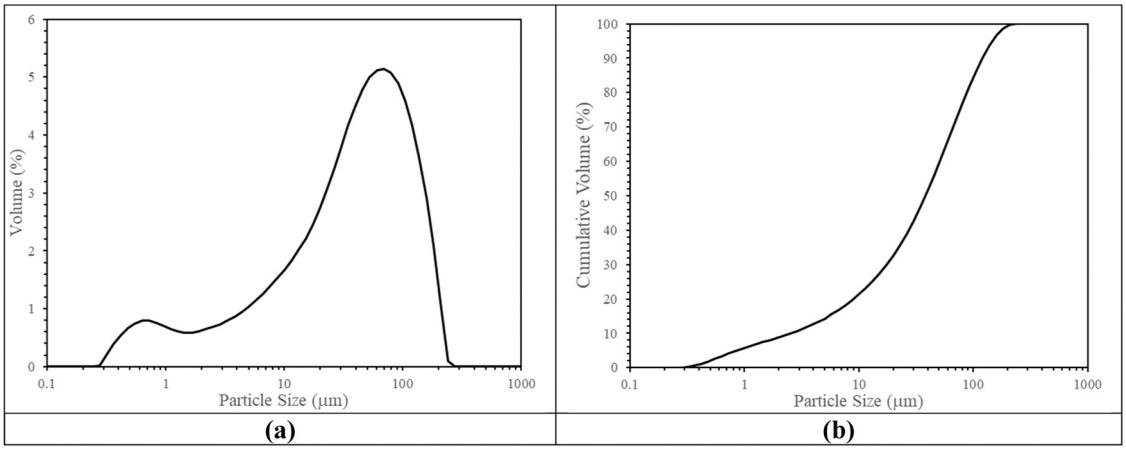

Fig. 2. a) Volumetric particle size distribution, b) Cumulative particle size distribution.

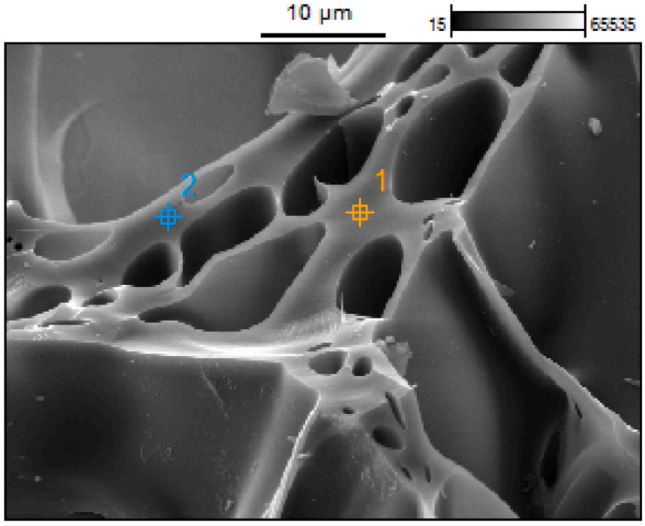

Fig. 3. SEM image of a NZ pumicite grain.

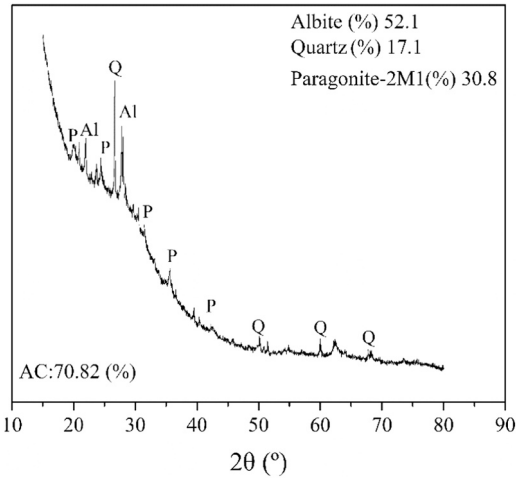

Fig. 4. XRD diffraction results of the NZ pumicite, Q: Quartz, Al: Albite, P: Paragonite.

Table 1
Chemical Composition (wt%) of New Zealand Pumicite from XRF Analysis.

SiO_2	Al_2O_3	Fe_2O_3	CaO	MgO	Na_2O	K_2O	TiO_2	LOI
74.0	14.0	1.0	1.3	0.3	3.0	4.0	0.1	2.5–3.2

[19]. Although NaOH is typically less expensive and has a lower carbon footprint during production, KOH is considered less harmful to the environment [40,41]. While this study focused solely on KOH and $NaAlO_2$ solutions, further research may be necessary to explore the impact of alternative activators on the strength and durability of the alkali-activated cement.

2.2. Experimental program

2.2.1. Mechanical treatment

Mechanical treatment (grinding) was performed using a Retsch Planetary Ball Mill PM to increase the specific surface area and, consequently, the reactivity of the pumicite. Since this process is time-dependent, different grinding durations were applied – 5, 10, and 20 minutes – at a constant rotating speed of 600 RPM.

2.2.2. Sample preparation

As shown in Table 2, the specimens were prepared in three groups of alkali-activated pastes to evaluate the effects of activator/pumicite (A/P) ratio, soluble aluminium, aging time, and curing temperature on the development of the alkali reaction. In Group I, the samples were designed to determine the optimum A/P ratio, with values ranging from 0.4, 0.5, and 0.6. Group II focused on assessing how soluble aluminium and aging time independently influence mechanical development at the optimum A/P ratio. Finally, Group III was established to examine the effect of curing temperature on the mechanical strength of the optimal mixture.

To prepare the pastes, the pumicite was directly mixed with the alkaline activators described in Table 2**.** The mixtures were blended using a desktop mixer for 10 minutes, after which the fresh paste was placed into 50×50×50 mm steel moulds in three layers. Each layer was compacted on a vibrating table for 30 seconds to expel air bubbles. The Syntron VP51 Vibrating Table was used for compaction, operating at 3600 vibrations per minute at 60 Hz, with an amplitude variation controller set to a maximum linear vibration of 1.6 mm. Finally, except for Group III, the moulds were sealed with two layers of food wrap and cured at 65°C for 72 hours.

After curing, the samples were extracted from the moulds and stored at room temperature with a relative humidity of 75–85 % until the designated time for the UCS test, as outlined in Table 2**.** The pastes from Group III were stored at room temperature until the scheduled testing age. The decision to compare curing conditions at elevated temperatures with room temperature curing is based on the assumption that room temperature significantly slows the alkali activation process. This comparison is essential for understanding the effect of temperature on the mechanical strength development of the pastes.

2.2.3. Compressive strength

The compressive strengths of the pastes were measured according to ASTM-C109/C109M−20 [42] using a strain-controlled universal testing machine (MTS Criterion C45.305–300 kN capacity) with a loading rate of 0.1 mm/min and a strain rate of 20 %. After four days of aging—representing early age response—samples cured at elevated temperatures were allowed to cool to room temperature for one day before testing. The samples were tested according to the aging times specified in Table 2. For each mixture, the test was conducted on three identical specimens, and the average results were reported.

2.2.4. Microstructural and characterisation tests

SEM/EDS analysis was conducted using a Hitachi SU-70 Schottky field emission scanning electron microscope with an accelerating voltage of 15 kV. The sample surfaces were coated with platinum for 100 seconds using a Hitachi E-1045 ion sputter to enhance electrical conductivity during SEM analysis. For EDS, the composition of particles was examined using a Noran System 7 (NSS) microanalysis system, with spot analysis performed at four points on each sample.

XRD patterns were recorded using a PANalytical Empyrean diffractometer with a Cu Kα-ray source and PIXcel 1D detector. The analysis was performed over a 2θ range of 20° to 80°, with a scan rate of 2°/min and a step size of 0.02°. FTIR spectra, ranging from 400 cm^{-1} to 4000 cm^{-1}, were also recorded using a Perkin Elmer Spectrum FTIR spectrometer equipped with an attenuated total reflectance (ATR) unit. FTIR was used to monitor aluminosilicate, hydroxyl, and carbonate bond transformations, given their significance in gel formation and mechanical development.

These analysis techniques were chosen due to their effectiveness in confirming pumicite's participation in the alkali activation process and the formation of amorphous high-Al and high-Si gels. This comprehensive analysis is essential for understanding the chemical and physical transformations in alkali-activated materials.

All samples for these analyses were taken from the tested specimens after Unconfined Compressive Strength (UCS) testing. To ensure consistency and accuracy, pieces were carefully selected from the centre of the cubic samples to minimise structural variations that could occur near the edges or corners. For SEM/EDS analysis, the smoother surface of each selected piece was oriented to face the electron beam for optimal imaging and elemental detection. The back side was secured to the SEM sample holder using epoxy glue. For

Table 2
Mixture proportions and experimental programme details.

	Samples	A/P (%)	Activator	KOH concentration (mol/L)	$NaAlO_2$ /KOH solution (weight ratio)	Compressive test	
						Curing condition	Age of samples (day)
Group I	PAL_i*	0.4,0.5, 0.6	K0	-	-	72 h@65°C	4
Group II	PALK1	0.5	K1	10	1	72 h@65°C	4, 28 and 56
	PALK3	0.5	K3	10	3	72 h@65°C	4, 28 and 56
	PALK5	0.5	K5	10	5	72 h@65°C	4, 28 and 56
	PAL	0.5	K0	-	-	72 h@65°C	4, 28 and 56
Group III	PALT	0.5	K0	-	-	72 h@65°C	4, 28 and 56
	PALR	0.5	K0	-	-	Room temperature	28 and 90

PAL_i: Pumicite +$NaAlO_2$ solution, * i= 0.4, 0.5, or 6, changing according to A/P ratio.
$PALK_j$: Pumicite +$NaAlO_2$ solution + KOH solution, * j= 1, 3, or 5, changing according to activator type.
PAL: Pumicite +$NaAlO_2$ solution.
PALT: Pumicite +$NaAlO_2$ solution + Elevated temperature.
PALR: Pumicite +$NaAlO_2$ solution + Room temperature.

XRD analysis, fragments were similarly taken from the central region of the samples and ground into fine powder to ensure uniformity, reducing the influence of particle size and orientation on the diffraction pattern.

3. Results and discussion

3.1. Effect of mechanical treatment on particle size distribution

Table 3 and Fig. 5 summarise the results of the mechanical treatment of pumicite through grinding. The particle size distribution curves obtained from LPSD for the unground pumicite and the samples ground for 5, 10, and 20 minutes are presented in Fig. 5. The curves for the ground samples shift to the left compared to the unground pumicite, indicating finer particle sizes. The ground pumicite particles range from 0.3 μm to 100 μm, while the unground pumicite particles vary between 0.3 μm and 250 μm. All ground samples display similar trends in the shape of the particle distribution curves, with several peaks between 2 μm and 45 μm. In contrast, the unground pumicite shows a single peak at 70 μm. This indicates that the grinding process not only reduced particle sizes but also produced a broader distribution of particle sizes.

The specific surface area (SSA) and BET-specific surface area were measured using LPSD and BET analyses, respectively. These results were used to determine the optimal grinding time for achieving maximum surface area and fine particle size. Mechanical treatment significantly affected the pumicite particles, with the ground samples exhibiting considerably smaller D50 and D90 values compared to the unground pumicite, due to the material's highly crushable and porous structure. As the grinding time increased to 20 minutes, a gradual decrease in particle size was observed. The SSA of the samples, measured by LPSD, increased steadily from 0.93 m^2/g to 1.97 m^2/g with 20 minutes of grinding.

Conversely, the BET analysis revealed a much higher surface area than SSA, which is attributed to the extensive internal surfaces within pumicite's pores that can only be captured by BET measurements. However, the BET surface area plateaued after 10 minutes of grinding. The rise in SSA is more significant than the increase in BET values, indicating that smaller particles with higher SSA exhibit less internal porosity, thereby improving their reactivity in alkaline activation.

These results indicate that ground pumicite has finer particle sizes and higher surface areas compared to the unground sample, with 20 minutes of grinding identified as the most effective in producing finer D10 and D50, as well as higher SSA and BET surface area.

3.2. Compressive strength

Fig. 6a and b show the early-age (4 days) stress-strain responses of all mixtures in Groups I and II, following 72 hours of curing at 65°C and 24 hours of cooling at room temperature. The results indicate that all pastes exhibited nearly linear stress-strain behaviour with brittle characteristics, as seen in the sudden drop in post-peak stresses. This observation aligns with findings from [43], where alkali-activated samples similarly demonstrated brittle behaviour. After reaching their ultimate strength, the samples fractured into triangular wedges, with concentrated fractures along the external surfaces (Fig. 6**c**), further indicating brittle failure.

Alkali-activated cements generally display more brittle behaviour compared to Portland cement-based systems due to the denser interfacial transition zone, higher binding strength, and increased tensile strength [44]. Additionally, alkaline activation tends to increase stiffness, as evidenced by the steeper slopes of the ascending branches in the stress-strain curves.

As expected, PALK1 exhibited the lowest early-age compressive strength (CS) at 26.95 MPa, while PAL0.4 showed the highest value of 60.96 MPa, followed closely by 59.35 MPa for PAL0.5. This significant difference in early-age strength can be attributed to the effect of soluble aluminium. Pumicite, as shown in Table 3, contains a higher silicate phase compared to aluminate. The shortage of aluminium in PALK1 contributed to its lower compressive strength, while samples in Group I activated by K0 achieved the highest early-age CS.

In a similar context, García-Lodeiro, *et al.* [45] successfully enhanced the alkali activation of calcined bentonites with a high SiO_2/Al_2O_3 ratio by adding commercial sodium aluminate and bauxite, releasing soluble aluminium from the bauxite. Additionally, rice husk ash, a silica-rich precursor, was reported to improve its alkaline reaction when an external source of aluminium was added [46].

More importantly, CS values measured in this study are significantly higher than those of pumice-based cement containing 35 % lime cured at 700°C for 4 hours with CS equal to 22 MPa [13]. Similarly, Hamid, *et al.* [47], reported a 26 MPa CS value for 100 % pumice-based alkali-activated cement after 4 days curing at 60ºC.

Table 3
Results of LPSD and BET Analyses for Unground and Ground Pumicite.

Grinding time (min)	0	5	10	20
D_{10} (μm)	2.90	1.38	1.37	1.10
D_{50} (μm)	43.80	9.04	7.78	6.67
D_{90} (μm)	137.2	43.52	40.57	44.82
BET Surface Area (m^2/g)	10.86	12.34	15.78	15.09
SSA (m^2/g)	0.93	1.57	1.62	1.97

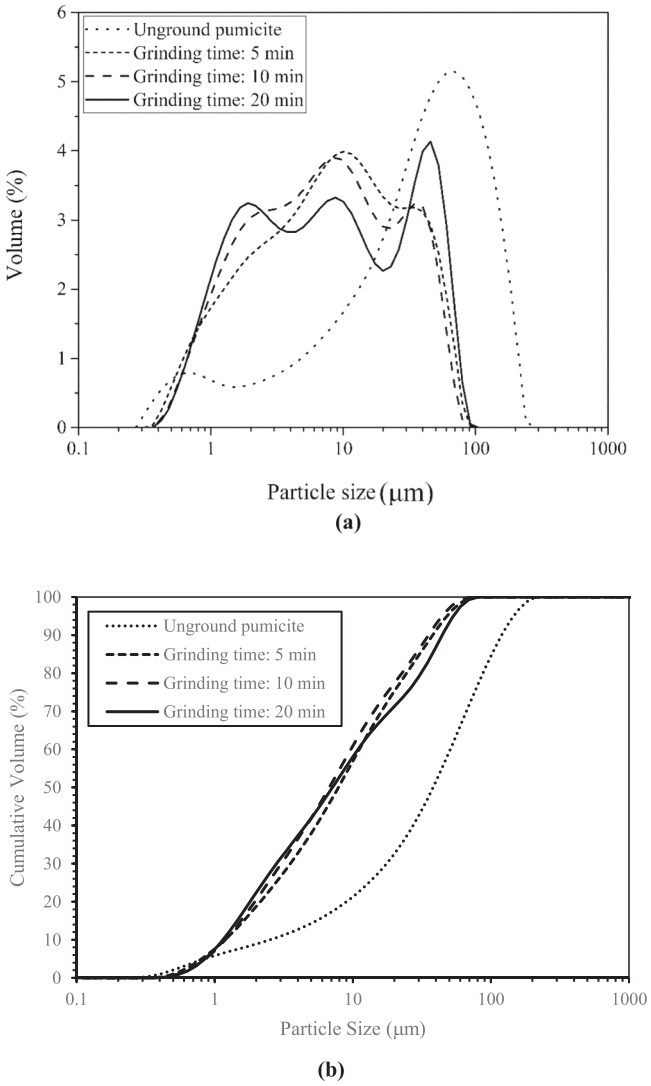

Fig. 5. (a) Volumetric and (b) cumulative volumetric particle size distribution curves obtained from LPSD for unground and pumicite ground for 5, 10, and 20 minutes.

3.2.1. The effect of A/P ratio

Fig. 7 illustrates the early-age compressive strength (CS) of pastes activated by $NaAlO_2$ solution (Group I) for various A/P ratios – 0.4, 0.5, and 0.6 – normalized against the value for PAL0.4. As expected, early-age CS values decreased from 61 MPa to 45 MPa as the A/P ratio increased from 0.4 to 0.6. A higher A/P ratio typically contributes to increased porosity with larger pores, which reduces compressive strength due to the lower formation of binding products [48,49]. However, only a slight decrease in early-age CS (~3 %) was observed when the A/P ratio increased from 0.4 to 0.5, while a more substantial drop occurred with a further increase in the A/P ratio.

Although A/P = 0.4 yielded the highest early-age CS of 61 MPa, A/P = 0.5 was selected for subsequent groups due to its positive impact on the paste's viscosity and workability [50], critical factors in cementitious pastes' development. This decision aligns with existing literature that reports an optimal A/P ratio of 0.46 for the alkali activation of 100 % pumice precursors, contributing to a CS of 26 MPa after 4 days of curing at 60°C [47].

Activator content significantly influences the strength development of alkali-activated materials, with an optimal dosage typically depending on the precursor type, alkali activators, and curing conditions [51]. According to Davidovits [8], dissolution begins with an alkaline attack progressing from the outside to the inside of the material. For higher A/P ratios, the contact between the alkaline solution and reactive solid phases is reduced due to the larger volume of fluid, which limits the dissolution and mobility of aluminosilicate phases through electrostatic shielding [52]. Conversely, a lower A/P ratio improves the dissolution and mobility of these phases. Excessive free water can dilute the matrix, lowering its alkalinity and slowing the dissolution process [43,53].

Thus, the A/P ratio controls strength development by influencing the interaction between the alkaline solution and solid phases, the

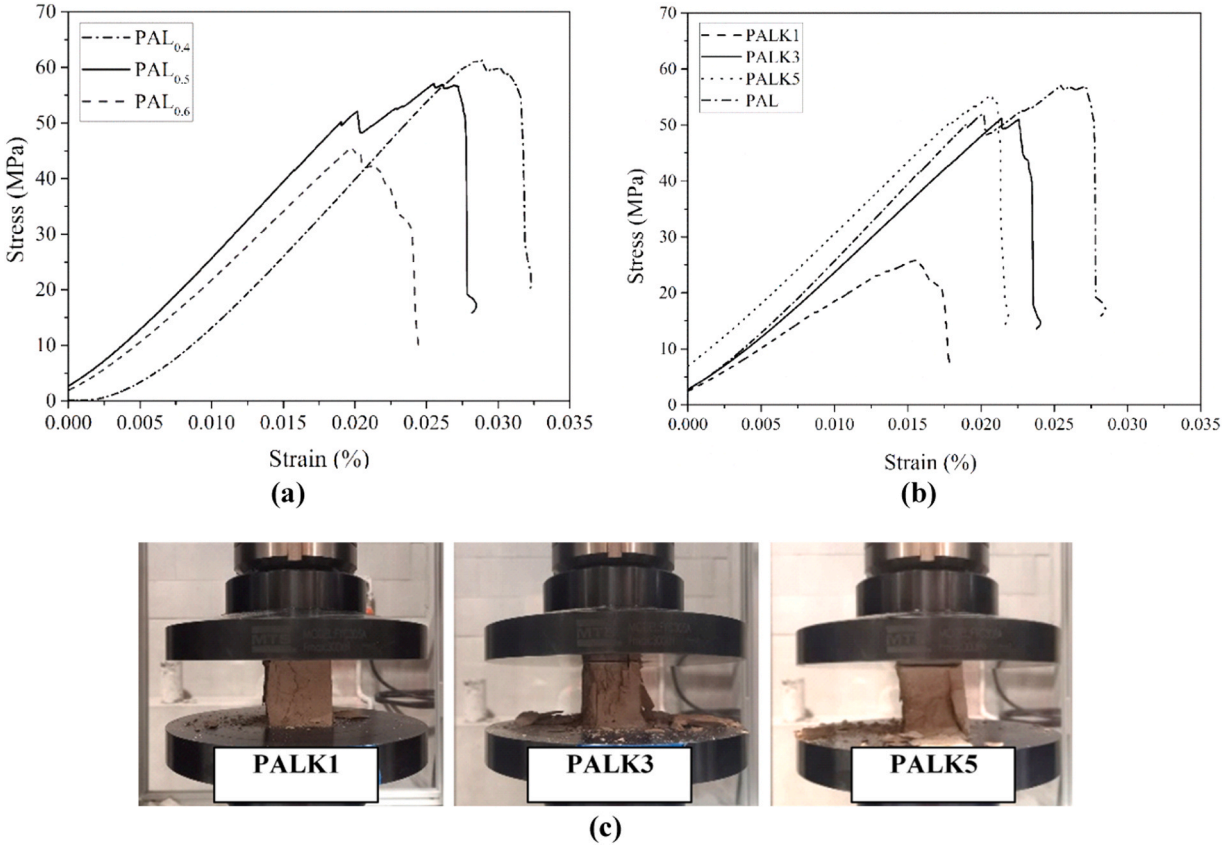

Fig. 6. Early-age stress-strain behaviour of the samples defined in (a) Group I, (b) Group II, (c) failure mode of the pastes prepared in Group II. PAL_i: Pumicite +$NaAlO_2$ Solution, * i= 0.4, 0.5, or 0.6, changing according to the A/P ratio. $PALK_j$: Pumicite +$NaAlO_2$ Solution + KOH solution, * j= 1, 3, or 5, changing according to activator type. PAL: Pumicite +$NaAlO_2$ Solution.

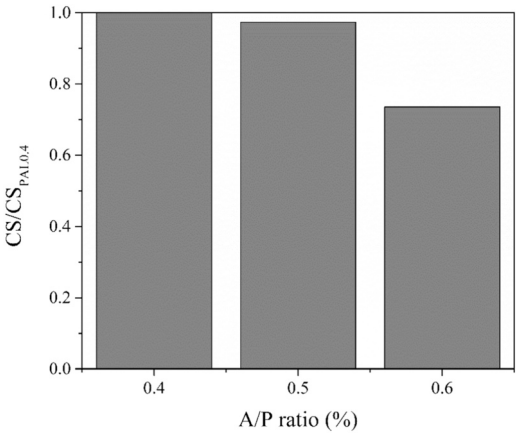

Fig. 7. Variations in early-age CS/CSPAL0.4 against A/P ratios for samples defined in Group I. *PAL_i: Pumicite +$NaAlO_2$ Solution, * i= 0.4, 0.5, or 0.6, changing according to the A/P ratio.*

matrix's alkalinity, and the dissolution and mobility of silica and alumina phases [52,54].

In the case of highly porous materials, the activator content initially fills the internal porosity to achieve saturation. Beyond this point, further increases in activator content reduce the contact between solid particles and the activator, limiting the mobility of aluminosilicate phases. This explains the comparable compressive strengths observed for pastes with A/P ratios of 0.4 and 0.5, where both ratios may exhibit a similar trend in terms of contact between the solid and the activator. However, an increase to an A/P ratio of

0.6 resulted in a 24.5 % decrease in compressive strength, attributed to reduced intermolecular contact.

The internal porosity of the pumicite, as shown in Fig. 2**b**, plays a role in the material's significant water adsorption capacity before reaching saturation. Upon wetting, the available fluid medium and free water are effectively reduced for A/P ratios from 0.4 to 0.5. However, a further increase in the A/P ratio by 10 % decreased intermolecular contacts and the mobility of aluminosilicate phases, leading to lower compressive strength [55]. Additionally, water released during the condensation stage of the alkali activation process, known as residual water, negatively impacts strength development by forming small pores within the matrix [33]. An A/P ratio higher than 0.5 also increased the amount of residual water, thus creating small pores that further reduced compressive strength.

The Al_2O_3 and Na_2O content from the alkaline activators generally increased as the A/P ratio rose, assuming a constant pumice weight. The Al_2O_3/Na_2O molar ratio of 1.34 suggests that each Na atom can bond with an Al atom to reach an equilibrium state. However, excess Al_2O_3 and Na_2O phases that do not participate in the alkali activation process may negatively impact the strength of the alkali-activated products [56]. This is further compounded by the increased influence of residual water and the fluid medium.

3.2.2. *The effect of activator compositions*

Fig. 8**a** shows the early-age compressive strength (CS) of the pastes in Group II, normalized against the corresponding value for PAL (CS_{PAL}). The data reveal a continuous increase in early-age CS with the addition of soluble aluminium, with PAL and PALK1 activated by K0 and K1 solutions showing the highest and lowest early-age CS values, respectively. The early-age CS of PALK1 is 44 % that of PAL, while PALK5 and PALK3 exhibit comparable early-age CS values, at 89 % and 82 % of the early-age CS_{max}, respectively.

This emphasizes the significant role of soluble aluminium in the alkali activation process and early-age strength development, as the condensation stages in the reaction are controlled by aluminium. With the adjustment of Si/Al ratios, the increase in soluble aluminium corresponding to the K3, K5, and K0 activators enhances early-age CS compared to K1, where insufficient aluminium limits the degree of alkali activation and condensation reactions [29,45]. It is well-established that a lack of reactive aluminium hinders the transformation of high-aluminium gels into high-silicon gels, negatively affecting mechanical strength [32].

Furthermore, the continuous increase in early-age CS with rising soluble aluminium content suggests that the potential negative effects of excess Al_2O_3 and Na_2O from higher activator content on early-age strength development were mitigated.

In contrast to the literature suggesting that Na^+ and K^+ ions promote alkali activation more effectively with a higher Si/Al ratio [5], this study found that higher K^+ content combined with lower soluble aluminium resulted in lower early-age compressive strength (CS) values. The sudden rise in the early-age CS of PALK3 compared to PALK1 can be attributed to the higher Na^+ concentration in PALK3, as well as the increased soluble aluminium content, which leads to the formation of stronger binding gels. The ionic size and hydration tendencies of Na^+ and K^+ play crucial roles in their coagulation behaviours. Na^+, with its smaller ionic radius and higher charge density, remains hydrated more effectively, while the larger K^+ is less intensely hydrated. This distinction explains why Na^+ favours gel formation due to stronger hydrogen bonding with silicates compared with K^+ [57].

3.2.3. *The effect of aging time*

Fig. 8**b** shows the variation in compressive strength (CS) values of the samples defined in Group II over different aging times. The data indicate that as aging time increased to 28 days, CS values generally decreased, with PAL and PALK5 experiencing the most significant losses. However, when the aging time was extended to 56 days, a different trend emerged, where CS values increased. In contrast, PALK1 and PALK3 continued to show reductions in CS, dropping from 26.95 MPa to 22.15 MPa and from 50.27 MPa to 33.63 MPa, respectively, over the same aging period. PALK5 exhibited a decline to 34.03 MPa after 28 days of aging, with only a modest increase of 4 MPa observed after 56 days.

In the case of PAL, the CS initially decreased from 59.35 MPa to 35.20 MPa after 28 days, but then nearly doubled to 67.2 MPa with

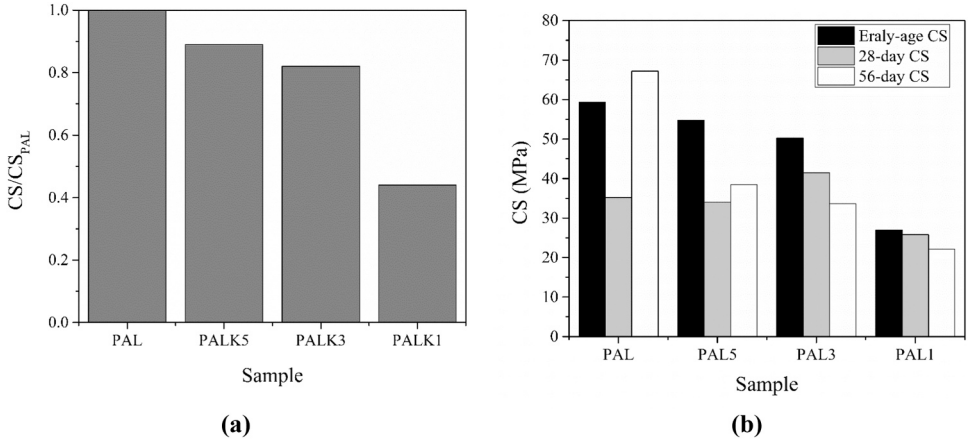

Fig. 8. a) Variations of early-age CS/CSPAL with A/P = 0.5, b) Variations of CS with aging time for the samples defined in Group II. *PAL_i: Pumicite +$NaAlO_2$ Solution, * i= 0.4, 0.5, or 0.6, changing according to A/P ratio. $PALK_j$: Pumicite +$NaAlO_2$ Solution + KOH solution, * j= 1, 3, or 5, changing according to activator type. PAL: Pumicite +$NaAlO_2$ Solution.*

extended aging to 56 days. Notably, the samples activated by K0 (PAL) showed an 8 MPa increase in CS after 56 days compared to their early-age values. It can be concluded that soluble aluminium in K0 improved early-age compressive strength (CS) and enhanced CS after 56 days of aging. In contrast, samples activated with binary solutions experienced a negative effect on CS development over longer aging times.

Despite the reduced CS values after 28 days, all samples still demonstrated significantly higher CS compared to pumice-based alkali-activated pastes activated by NaOH and Na_2SiO_3, which reported a compressive strength of around 3.5 MPa after curing at 60°C for 48 hours and at 28 days of age [34]. The CS of PAL was almost ten times higher than the values reported in that study [34]. This suggests that $NaAlO_2$-based solutions performed significantly better than the combination of NaOH and Na_2SiO_3, likely due to the availability of more aluminium phases that promote alkali activation.

As a general explanation of the findings, high aluminium content accelerates the condensation of aluminate and silicate, resulting in higher early-age compressive strength and increased crystallinity in the reaction products [56,58]. The availability of soluble aluminium promotes the formation of Al-rich N-A-S-H gels, which eventually transform into Si-rich gels over time. These Si-rich gels are crucial for long-term mechanical development [32]. The easy access to aluminium on the pumicite surfaces facilitates silica dissolution, but aging at room temperature slows the dissolution of silica phases [59,60]. As a result, the shortage of silica species hinders the formation of Si-rich gels, leading to an excess of Al-rich gels.

These Al-rich gels are prone to chemical expansion, which negatively affects the mechanical strength of the pastes after 28 days of aging [61]. With higher soluble aluminium, the compressive strength of the samples decreased due to the formation of more Al-rich gels, which are short-range-ordered and have a lower degree of condensation [56,62]. However, prolonged aging to 56 days enhanced the dissolution of the precursor and facilitated the evolution of Al-rich gels into Si-rich gels. This effect was most pronounced in PAL, where the higher availability of soluble aluminium led to the formation of more binding gels. These binding gels in PAL may have mitigated the chemical expansion caused by Al-rich gels, contributing to the increased mechanical strength, followed by PALK5.

3.2.4. *The effect of curing temperature*

Fig. 9 illustrates how curing temperature affected the alkaline reaction of PAL, identified as the best-performing mixture in this study. The results highlight the significant impact of elevated temperature on mechanical strength development and the shortening of aging time. The maximum compressive strength (CS) of PALT, observed after 56 days of aging (67.2 MPa), is significantly higher than that of PALR, which reached 36.50 MPa after 90 days. More importantly, the 28-day CS of PALR is minimal compared to PALT. In comparison, Occhipinti, *et al.* [63] reported a CS of 12 MPa for an Aeolian pumice-based geopolymer mixed with 20–30 wt% of metakaolin after 28 days of curing, where the raw pumice was dry milled to a grain size of less than 75 μm.

PALR eventually achieved a CS of around 36.50 MPa after 90 days of aging, while PALT attained a similar CS value after just 28 days of curing. This indicates that curing at room temperature requires almost three times the aging time at 65°C to achieve similar strength. In line with these findings, Lemougna, *et al.* [64] reported that 100 % volcanic ash samples were still soft after 7 days at 25°C, comparable to room temperature curing. Similarly, Safari, *et al.* [65] found that curing at 60°C for 72 hours was sufficient to produce a sustainable pumice-based geopolymer, with longer curing times gradually decreasing strength.

Curing at elevated temperatures increases the alkalinity of the matrix by accelerating the evaporation of residual water, while the dissolution of aluminosilicate phases and the development of condensation processes require a longer time at room temperature [33]. This highlights the significant influence of temperature on the mechanical behaviour of pumicite-based alkali-activated paste and the importance of extended aging when curing at lower temperatures. Elevated temperatures accelerate chemical reactions [66] and promote the dissolution of Si and Al phases [67]. Increasing the interaction between aluminosilicate phases and the alkaline activator

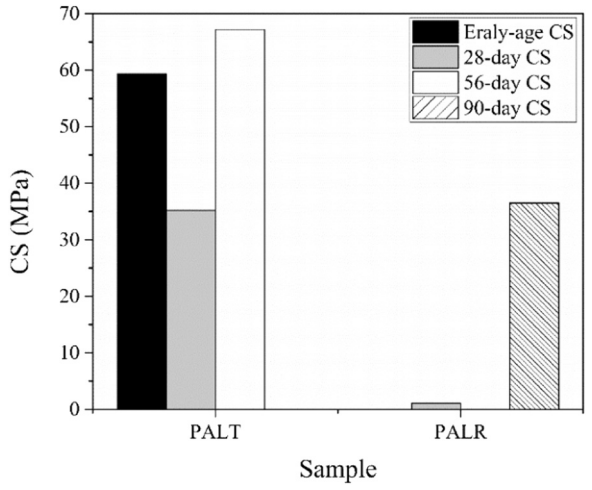

Fig. 9. Variations in compressive strength (CS) for samples in Group III, comparing room temperature curing and elevated temperature curing (65°C). *PALT: Pumicite +$NaAlO_2$ Solution + Elevated temperature, PALR: Pumicite +$NaAlO_2$ Solution + Room temperature.*

[68] leads to higher mechanical strength in a shorter aging time, however, longer aging is necessary when an elevated temperature is absent.

Prolonged aging enhances the interaction between the alkaline activator and aluminosilicate phases, promoting both dissolution

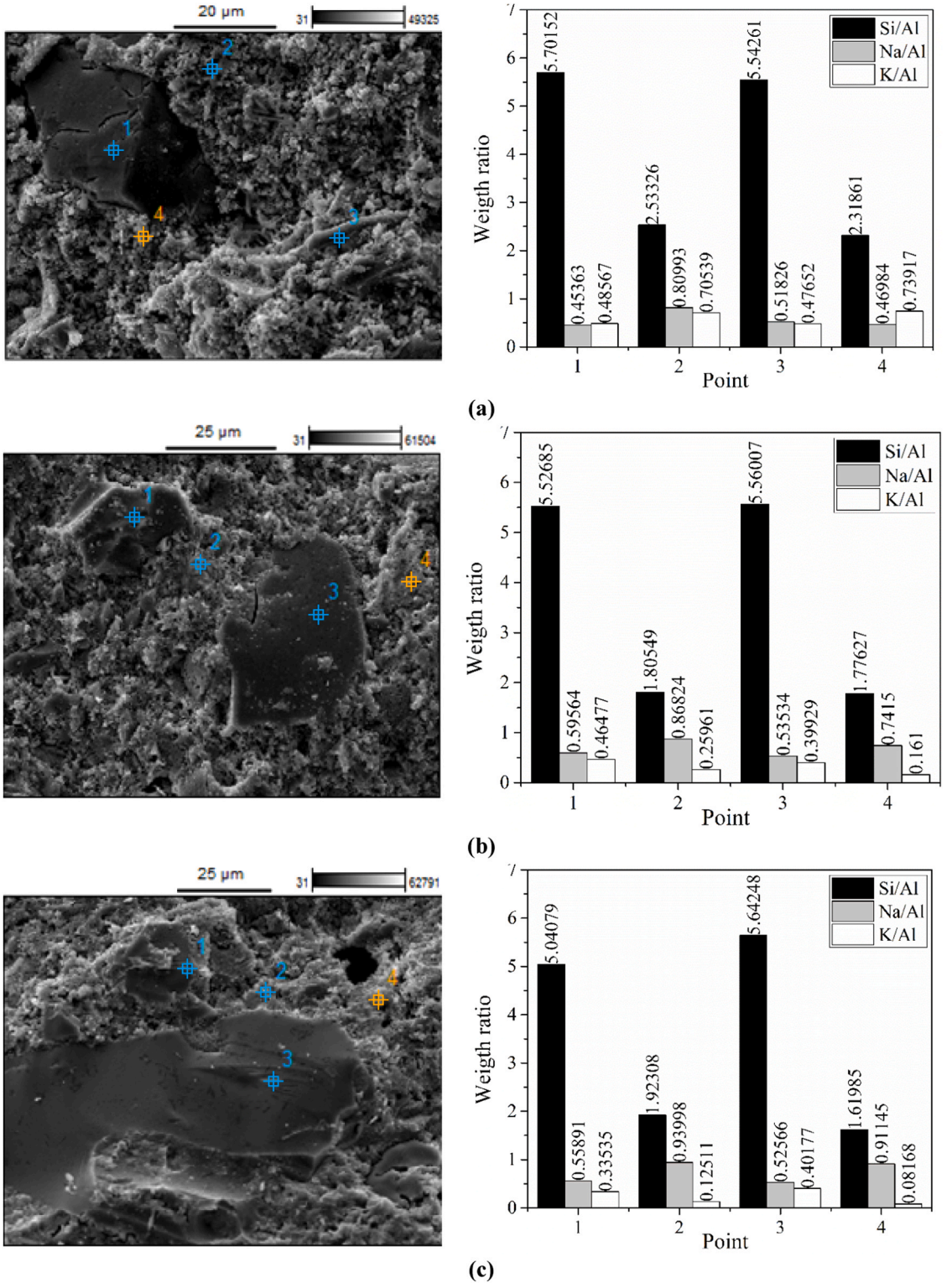

Fig. 10. SEM/EDS results of a) PALK1, b) PALK5, and c) PAL, after 4 days of aging.

and condensation processes [69]. The substantial difference in compressive strength (CS) values regarding curing temperature can be attributed to the significant effect of pumicite's internal porosity, which requires longer aging times to fully engage in alkaline reactions at ambient temperatures. In contrast, higher temperatures accelerate these interactions. The comparison between the SSA and

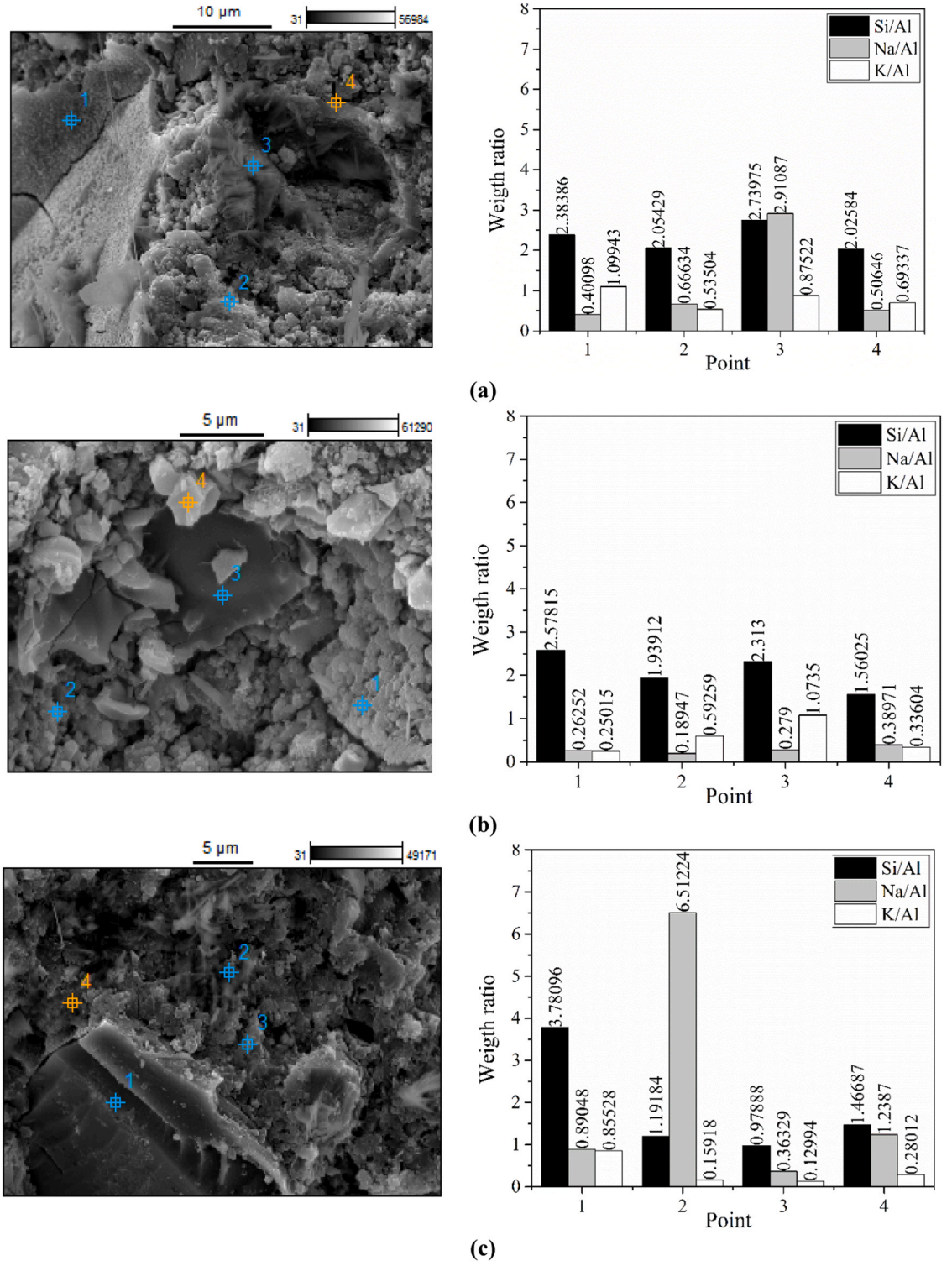

Fig. 11. SEM/EDS results of a) early-age PALK1, b) 56-day-aged PALK1, c) early-age PALK5, d) 56-day-aged PALK5, e) early-age PAL, and f) 56-day-aged PAL.

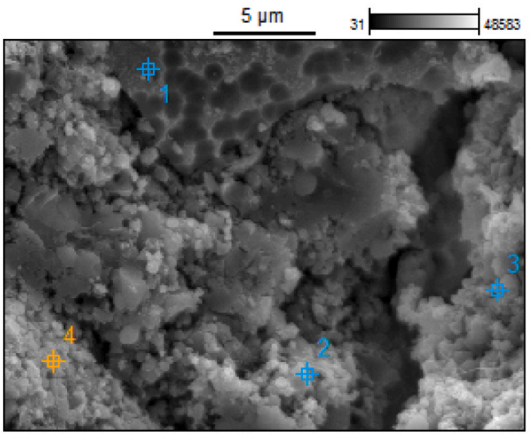

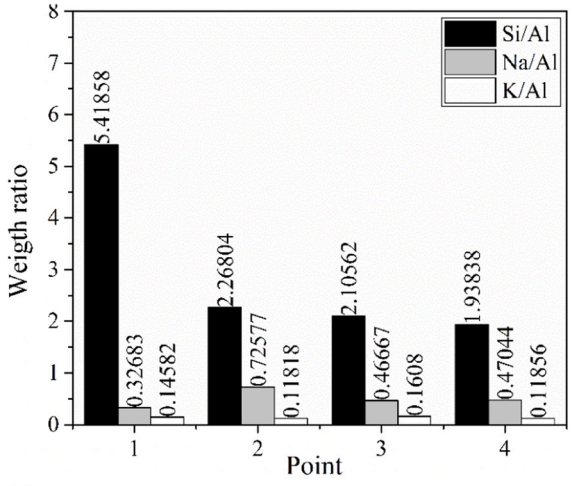

(d)

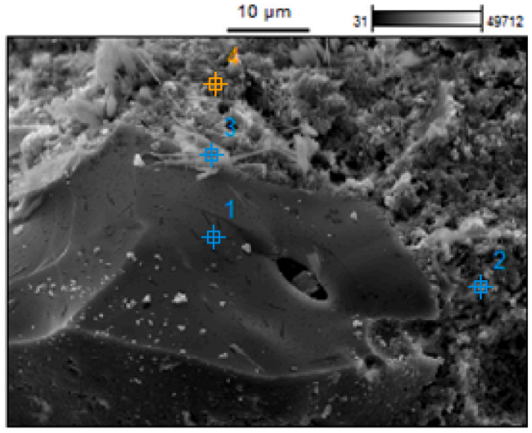

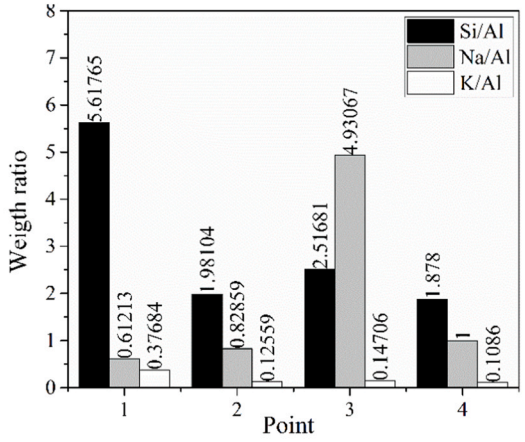

(e)

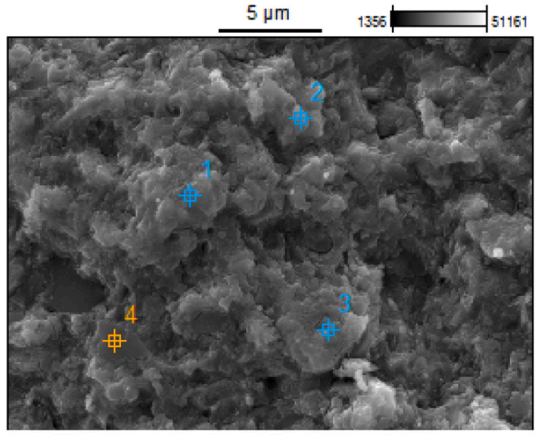

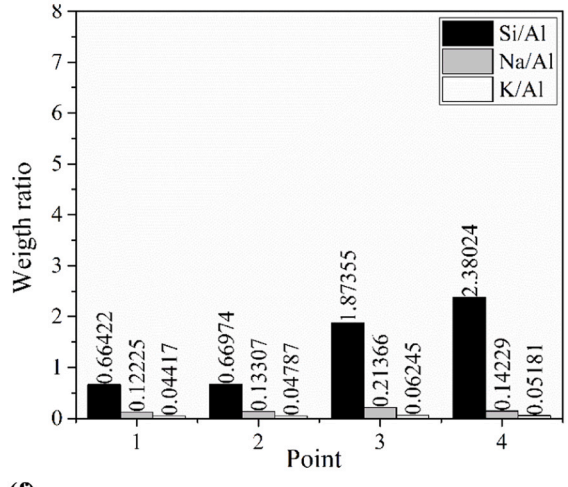

(f)

Fig. 11. (*continued*).

BET-specific surface areas of pumicite reveals that a significant portion of the surface area is controlled by internal porosity, which may considerably reduce the rate of alkali activation at room temperature.

The energy implications of elevated temperature curing involve increased energy consumption due to the need for external heating. However, this method often results in faster production and superior material properties. In contrast, room temperature curing is more

energy-efficient but requires extended curing times and may not always achieve the same level of material performance. The decision between these methods depends on the specific application requirements, where factors such as energy efficiency, material performance, production speed, and environmental impact must be carefully balanced.

Interestingly, no evidence of efflorescence formation was observed in the pastes cured at room temperature, even after extended aging. This could be attributed to the addition of soluble aluminium, as the presence of Al-rich materials and elevated curing temperatures are known to suppress the formation of efflorescence [70].

3.3. Microstructural and characterisation analysis

3.3.1. SEM/EDS analysis

Fig. 10 illustrates the SEM/EDS results of PALK1, PALK5, and PAL after 4 days of aging. The formation of powder-like morphology, identified as N-A-S-H gels, is evident in all three samples, with unreacted pumicite particles surrounded by fine clusters of aluminosilicate gels. Fig. 10a shows that PALK1 exhibits the highest porosity among the three pastes, followed by PALK5 in Fig. 10b. In contrast, Fig. 10**c** (PAL) presents the most condensed structure. The higher porosity in PALK1 and PALK5 is believed to weaken the cementitious matrix, which correlates well with the compressive strength test results.

Fig. 10 also presents the variations in Si/Al, Na/Al, and K/Al ratios based on the EDS results. All three pastes showed Si/Al ratios greater than 5 at points 1 and 3 (unreacted pumicite), which is significantly higher than the optimal Si/Al ratio range of 1.5–2.0 for N-A-S-H gel formation [71]. The aluminosilicate gels observed at points 2 and 4 exhibited a notable reduction in the Si/Al ratio. This indicates the high Si and low Al content in pumicite, underscoring the need for additional soluble Al to form N-A-S-H gels. As a result, the gels produced had significantly lower Si/Al ratios compared to the pumicite.

PALK1, with Si/Al ratios of 2.5 and 2.3, exhibited the lowest compressive strength, while PALK5 and PAL, with Si/Al ratios between 1.5 and 2.0, showed significant increases in compressive strength. This demonstrates the effectiveness of adding soluble Al to adjust the Si/Al ratio and promote alkali activation reactions. The Si/Al ratio of 1.92 observed at point 2 in PAL aligns well with the literature [71], which reports that an optimal Si/Al ratio close to 2 results in peak compressive strength, while further increases in this ratio lead to a reduction in strength.

Regarding the K/Al and Na/Al ratios, it can be concluded that both K^+ and Na^+ precipitated into the alkali-activated gels to balance the available $[AlO_4]^{5-}$ tetrahedrons. K^+ was detected at points 2 and 4 in all three binders, with the highest presence in PALK1, followed by PALK5 and PAL. Although KOH solution was not used in PAL, the presence of K^+ originated from the pumicite, as indicated by measurements at points 1 and 3. The sum of the Na/Al and K/Al ratios exceeding one suggests that all $[AlO_4]^{5-}$ tetrahedrons were balanced by alkali cations [72].

Additionally, as the proportion of $NaAlO_2$ increased, along with higher Na_2O and Al_2O_3 phases, the (Na+K)/Al ratio in the aluminosilicate gels decreased, while the corresponding value for the unreacted pumicite remained almost constant. PALK1 exhibited a (Na+K)/Al ratio ranging from 1.5 to 1.2, followed by PALK5 with values of 1.127 and 0.9, and PAL with 1.064 and 0.99, indicating increased adsorption of alkali ions. These findings align with the literature, where a Na/Al ratio of 1 is associated with optimal gel formation [72,73], and a high Si/Al ratio requires a Na/Al ratio of at least 1 for improved performance [73].

Fig. 11**a** shows a high uptake of Na at point 3 in PALK1, indicating zeolite formation. In the case of PALK5 (Fig. 11**c**), the Si/Al ratio of less than 1 at point 3 suggests the presence of Al-rich gels, while the high Na content at point 2 refers to unreacted NaOH, with a needle-like morphology. Point 4, characterized by high Si and Na uptake, indicates the formation of zeolite-like secondary products.

For PAL, point 3 again reveals unreacted NaOH, as indicated by both its morphology and the high Na content. The presence of unreacted NaOH phases in both PALK5 and PAL is attributed to the $NaAlO_2$ content. Moreover, in both PALK5 and PAL, the

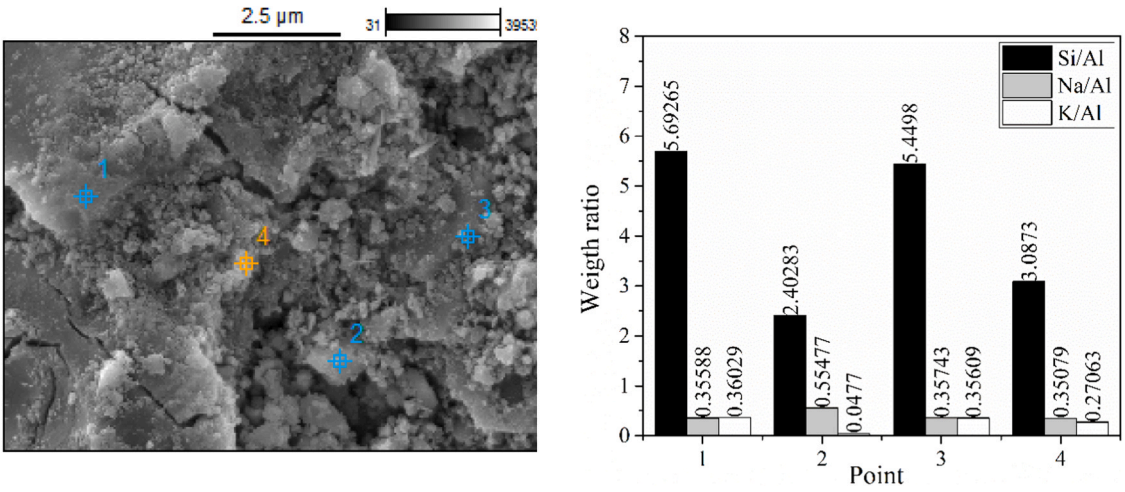

Fig. 12. SEM/EDS results of PALR after 90 days of aging.

morphology at point 1 shows unreacted pumicite. While PAL follows the Si/Al ratio of pumicite as seen in Fig. 10, PALK5 displays a lower Si/Al ratio of 3.78, indicating partial dissolution.

Regarding the effect of prolonged aging time, Fig. 11b reveals a discrete matrix with intraparticle gaps and a less connected morphology compared to Fig. 11a, confirming the drop in compressive strength (CS) as aging time increases. The 56-day-aged PALK1 showed a lower Si/Al ratio compared to its early-age counterpart, indicating reduced Si precipitation into the final products, such as Al-rich gels. The morphology in Fig. 11d exhibited more granular and homogeneous particles, likely aluminosilicate gels, though with higher porosity and a less connected structure compared to Fig. 11c. However, the Si/Al ratios remained within the optimal range.

More importantly, the comparison between Fig. 11e and f clearly illustrates a more uniform and well-connected matrix of binding gels after 56 days of aging, effectively bridging small porosities and correlating with the observed rise in CS values. Although points 1 and 2 show increased Al content in the final products, the Si/Al ratios at points 3 and 4 indicate the presence of high-Si gels, aligning with the optimal Si/Al ratio. Furthermore, the Na/Al ratio decreased with prolonged aging, suggesting increased incorporation of Al into aluminosilicate gels. No evidence of zeolite formation or excess Na^{+} was observed in the samples after 56 days of aging at room temperature.

Fig. 12 reveals the morphology of PALR after 90 days of aging, where numerous unreacted pumicite particles and less connected N-A-S-H gels are visible. Points 1 and 3 correspond to unreacted pumicite with Si/Al ratios greater than 5, while points 2 and 4 represent aluminosilicate gels with Si/Al ratios of 2.402 and 3.087, respectively – both higher than those observed in Fig. 9 – indicating lower aluminium precipitation in the aluminosilicate gels. The low compressive strength (CS) of PALR is further confirmed by the presence of micro-cracking and poorly connected binding gels. No evidence of zeolite formation was observed. As expected, the primary products of the alkali activation reaction at room temperature are amorphous N-A-S-H gels [58].

SEM/EDS analyses reveal the microstructural changes, including the evolution of high-Al or high-Si gels, that contribute to variations in compressive strength across different activator compositions and curing conditions in Groups II and III. The Si/Al and Na/Al ratios, ranging from 1.5 to 2.0 and 1.064–0.99, respectively, were associated with the maximum compressive strength measured for PAL. Prolonged aging to 56 days resulted in a transformation to a uniform and well-connected matrix of binding gels, with no evidence of unreacted pumicite remaining.

3.3.2. XRD analysis

Fig. 13 shows the XRD patterns of PAL, PALK1, and PALK5 after 4 days of aging. The XRD patterns display a hump between the 2θ values of 25° and 35°, compared to raw pumicite, indicating the formation of amorphous gels. In addition to albite and quartz, new crystalline phases, including gibbsite and zeolite-A, were observed in all three alkali-activated samples. Zeolite-A contributes significantly to the formation of aluminosilicate gels within the pastes, with a substantial crystalline phase percentage in PAL (59.7 %), compared to PALK1 (39 %) and PALK5 (38 %).

Gibbsite ($Al(OH)_3$), varying from 4.5 % to 11.7 %, represents soluble aluminium that did not participate in the alkali activation process. The disappearance of paragonite further suggests the restructuring of the original crystalline phases due to the alkaline reaction. Additionally, the reduced percentages of albite and quartz with increased soluble Al in the alkali-activated pumicite, compared to raw pumicite, indicate the positive role of soluble Al in promoting phase dissolution and transformation.

In general, the amorphous content decreased with the increase in soluble Al, leading to a reduction in the amorphous content of PAL and PALK5 to 58.10 % and 64.10 %, respectively—both lower than that of the raw pumicite, which was 70.82 %. This decrease

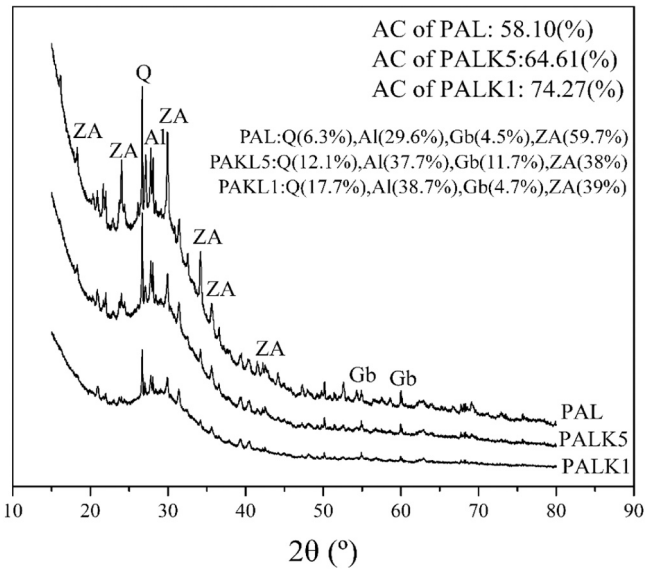

Fig. 13. XRD diffraction results of PAL, PALK1, and PALK5 after 4 days of aging. Q: Quartz, Al: Albite, Gb: Gibbsite, ZA: Zeolite-A.

can be attributed to the easy access to soluble Al during the gel formation process, which promotes increased crystallinity [56]. These findings align with observations made by Gluth, *et al.* [74], where an amorphous gel and zeolite-A were identified as the main reaction products when sodium aluminate was used as the activator.

XRD patterns confirm the transformation of crystalline phases, such as the formation of zeolite, which correlates with compressive strength development in Group II. The comparison of XRD patterns shows that PAL contained the lowest levels of quartz, albite, and gibbsite compared to PALK1 and PALK5 while exhibiting a higher percentage of zeolite-A. In line with the compressive strength results, this may be attributed to the increased consumption of Al and Si phases to produce aluminosilicate gels, thereby contributing to the formation of zeolite-A.

3.3.3. FTIR analysis

FTIR spectra of the raw pumicite, PALK1, PALK5, and PAL after 4 days of aging are presented in a wide range of 500–4000 cm^{-1} and a zoomed-in range of 450–2000 cm^{-1} in Fig. 14a and b, respectively. In line with the XRD results, the peak at 784.82 cm^{-1}, corresponding to Si-O-Si stretching in pumicite and associated with quartz [75,76], shifted to lower frequencies in all three pastes. This shift

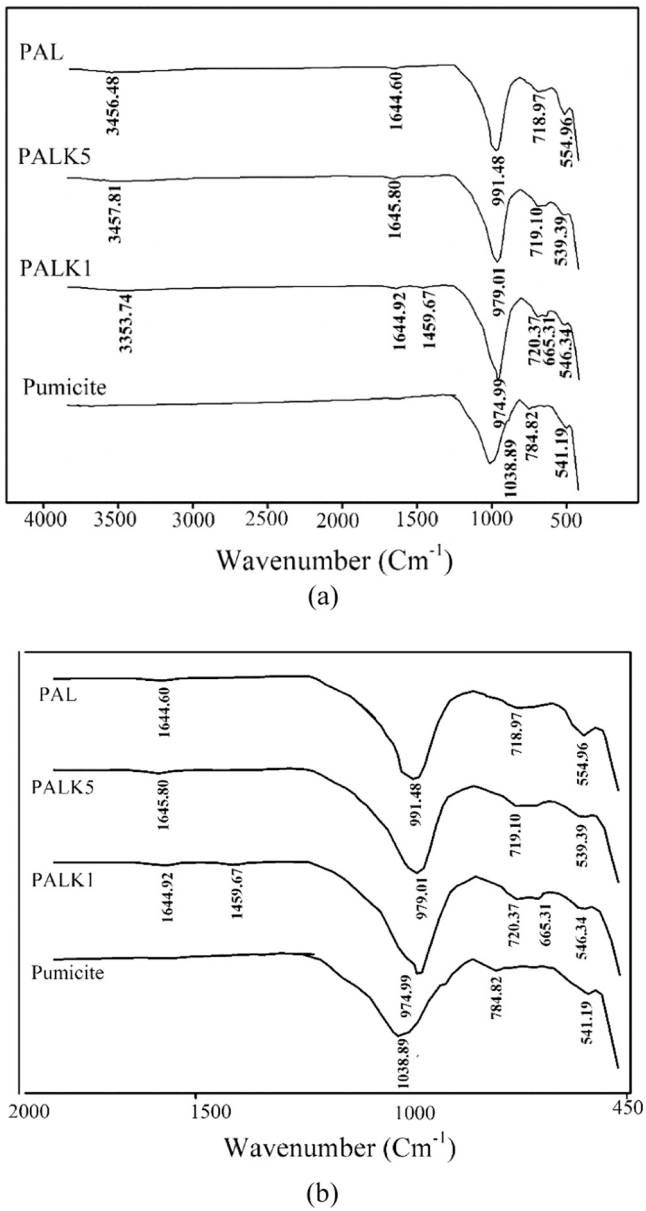

Fig. 14. FTIR spectra of raw pumicite, PALK1, PALK5, and PAL after 4 days of aging, shown in the ranges of (a) 500–4000 cm^{-1} and (b) 450–2000 cm^{-1}.

indicates the dissolution and reorganization of Si-O bonds in the alkali-activated pastes [8].

The frequency at 1038.89 cm^{-1}, indicating Si-O stretching in the raw pumicite [76], shifted to lower frequencies of 974.99 cm^{-1}, 979.01 cm^{-1}, and 991.48 cm^{-1} in PALK1, PALK5, and PAL, respectively, which is attributed to Al (IV)-OH bonds [77]. This transformation from Si-O to Al-OH bonds is the primary reason for the formation of high-aluminate gels in the pastes and represents the main distinction between the original pumicite and the alkali-activated pastes [63]. Notably, the higher frequencies observed in PALK5 and PAL (979.01 cm^{-1} and 991.48 cm^{-1}) correspond with their superior compressive strength compared to PALK1.

The peak at 541 cm^{-1}, referring to Si–O–Al bonds where Al is in octahedral coordination [78], shifts to higher frequencies, particularly in PAL (554.96 cm^{-1}) [76]. This shift indicates an increase in aluminosilicate bonds, which correlates with the higher unconfined compressive strength (UCS) values observed for PAL.

Additionally, the peaks observed in PALK5 and PAL appeared at higher frequencies (979.01 cm^{-1} and 991.48 cm^{-1}, respectively) compared to PALK1 (974.99 cm^{-1}), indicating higher crystallinity. The intensity of the corresponding bonds was reduced in the pastes relative to the raw pumicite, suggesting a lower population of bonds due to the dissolution or alteration of the molecular structure of solid silica.

FTIR spectra demonstrate chemical transformations, including shifts from Si-O to Al-OH bonds, validating the enhanced gel formation observed in SEM/EDS and the corresponding mechanical strength improvements in Group II. Peaks between 1644 cm^{-1} and 1645 cm^{-1}, and between 3350 cm^{-1} and 3460 cm^{-1}, correspond to OH deformation and water molecule stretching, respectively [76, 79]. These peaks indicate the transformation of adsorbed water into structural water within the binding agents, which is essential for gel formation. Additionally, the frequency at 665.31 cm^{-1} observed in PALK1 reflects Si-O-Al symmetric stretching, signifying the presence of more amorphous gels [78], This supports the observation that PALK1 contains the highest proportion of amorphous phases among the samples.

4. Conclusions

This research evaluated how aluminate-based activators enhance the reactivity of New Zealand pumicite through alkali activation. Increasing the A/P ratio from 0.4 to 0.5 maintained compressive strength due to water adsorption from high porosity. However, a further increase to 0.6 reduced strength, limiting intermolecular contact and aluminosilicate mobility. Pure $NaAlO_2$ solution effectively adjusted the Si/Al ratio to 2, promoting activation.

SEM/EDS revealed that Al-rich N-A-S-H gels initially reduced strength at room temperature after 28 days, but prolonged aging transformed them into Si-rich gels. Results also indicated that room temperature curing required three times longer than 65°C for similar strength. Microstructural analyses also confirmed improved activation due to soluble aluminium. FTIR showed Si-O shifting to Al-OH bonds, forming high-aluminate gels after 4 days. SEM/EDS revealed high-Si gels over time, with XRD identifying zeolite-A formation, consistent with SEM/EDS results.

The successful use of New Zealand pumicite in developing an alkali-activated cement highlights its potential as a sustainable alternative to traditional cementitious materials, particularly in regions rich in pumice. Moreover, reducing the carbon footprint of cement production by utilising locally sourced materials supports the broader adoption of the pumicite-based binder. Further studies could explore the long-term durability of this material under diverse environmental conditions. It is also necessary to investigate the scalability and assess the economic and environmental impacts of large-scale production of this binder.

Financial support

This research was supported by the Faculty of Design and Creative Technology (DCT) at Auckland University of Technology (AUT), New Zealand, through project funds R12353.16 and R12679.10, titled “An Environmentally Friendly Alkali-activated Volcanic Ash Binder” and “Developing a Low-Carbon Volcanic Grout for Ground Stabilisation Based on New Zealand Natural Pozzolans”, respectively. The financial support from DCT primarily facilitated the procurement of materials and equipment for laboratory tests. The DCT Faculty was not involved in the study design, data collection, analysis, interpretation, report writing, or the decision to submit this article for publication.

CRediT authorship contribution statement

Roohollah Kalatehjari: Writing – review & editing, Writing – original draft, Visualization, Validation, Supervision, Software, Resources, Project administration, Methodology, Funding acquisition, Formal analysis, Data curation, Conceptualization. **Elmira Khaksar Najafi:** Writing – review & editing, Writing – original draft, Visualization, Validation, Methodology, Investigation, Formal analysis, Data curation. **Afshin Asadi:** Writing – review & editing, Writing – original draft, Supervision, Software, Project administration, Methodology, Investigation, Funding acquisition, Formal analysis, Conceptualization. **Martin Brook:** Writing – review & editing, Writing – original draft, Visualization, Investigation.

Declaration of Competing Interest

The authors declare that they have no known competing financial interests or personal relationships that could have appeared to influence the work reported in this paper.

Acknowledgment

The authors appreciate Yousef Adeeb Chamachaei, Sara Bayandor, and Ava Asadi for their crucial contributions and dedication, which were pivotal to the success of this work.

Data availability

No data was used for the research described in the article.

References

[1] P.-C. Aïtcin, Cements of yesterday and today: concrete of tomorrow, Cem. Concr. Res. 30 (2000) 1349–1359.
[2] R.M. Andrew, Global CO 2 emissions from cement production, Earth Syst. Sci. Data 10 (2018) 195–217.
[3] de Coninck, H.; Revi, A.; Babiker, M.; Bertoldi, P.; Buckeridge, M.; Cartwright, A.; Dong, W.; Ford, J.; Fuss, S.; Hourcade, J.-C. Strengthening and implementing the global response. 2018.
[4] A.F. Abdalqader, F. Jin, A. Al-Tabbaa, Development of greener alkali-activated cement: utilisation of sodium carbonate for activating slag and fly ash mixtures, J. Clean. Prod. 113 (2016) 66–75.
[5] P. Duxson, S.W. Mallicoat, G.C. Lukey, W.M. Kriven, J.S. Van Deventer, The effect of alkali and Si/Al ratio on the development of mechanical properties of metakaolin-based geopolymers, Colloids Surf. A: Physicochem. Eng. Asp. 292 (2007) 8–20.
[6] K.-H. Yang, J.-K. Song, K.-I. Song, Assessment of CO2 reduction of alkali-activated concrete, J. Clean. Prod. 39 (2013) 265–272.
[7] A.J. Klemm, R. Rostami, S. MacLennan, F. Almeida, Supplementary cementitious materials and their impact on sustainable construction, in: Proceedings of the Brittle Matrix Composites 12-Proceedings of the 12th International Symposium on Brittle Matrix Composites, 2019, BMC, 2019, pp. 127–137.
[8] J. Davidovits. Geopolymer Chemistry and Applications, fifth ed., Institut Géopolymère, France, 2020.
[9] N. Mobasher, S.A. Bernal, J.L. Provis, Structural evolution of an alkali sulfate activated slag cement, J. Nucl. Mater. 468 (2016) 97–104.
[10] F. Pacheco-Torgal, J. Castro-Gomes, S. Jalali, Alkali-activated binders: a review: Part 1. Historical background, terminology, reaction mechanisms and hydration products, Constr. Build. Mater. 22 (2008) 1305–1314.
[11] A.Z. Khalifa, Ö. Cizer, Y. Pontikes, A. Heath, P. Patureau, S.A. Bernal, A.T. Marsh, Advances in alkali-activation of clay minerals, Cem. Concr. Res. 132 (2020) 106050.
[12] J.L. Provis, J.S.J. Van Deventer, Geopolymers: structures, processing, properties and industrial applications, Elsevier, 2009.
[13] A.T. Almalkawi, S. Hamadna, P. Soroushian, One-part alkali activated cement based volcanic pumice, Constr. Build. Mater. 152 (2017) 367–374.
[14] C. Bagci, D. Kafkas, D.M. Samuel, W.M. Kriven, Sustainable activation of pumice with partially variable substitutions of metakaolin and/or fumed silica, Int. J. Appl. Ceram. Technol. (2023).
[15] B. Balun, M. Karataş, Influence of curing conditions on pumice-based alkali activated composites incorporating Portland cement, J. Build. Eng. 43 (2021) 102605.
[16] K. Cabrera-Luna, P. Perez-Cortes, J.E. Garcia, Influence of quicklime and Portland cement, as alkaline activators, on the reaction products of supersulfated cements based on pumice, Cem. Concr. Compos. 146 (2024) 105379.
[17] J.N.Y. Djobo, A. Elimbi, H.K. Tchakouté, S. Kumar, Reactivity of volcanic ash in alkaline medium, microstructural and strength characteristics of resulting geopolymers under different synthesis conditions, J. Mater. Sci. 51 (2016) 10301–10317.
[18] A. Játiva, E. Ruales, M. Etxeberria, Volcanic ash as a sustainable binder material: an extensive review, Materials 14 (2021) 1302.
[19] N. Kabay, M. Mert, N. Miyan, T. Omur, Pumice as precursor in geopolymer paste and mortar, J. Civ. Eng. Constr. 10 (2021) 225–236.
[20] J. Lopez-Salas, J.I. Escalante-Garcia, Hybrid binders based on volcanic pumice: effect of the chemical composition on strength and microstructures, Cem. Concr. Res. 176 (2024) 107393.
[21] R. Occhipinti, G. Lanzafame, A.L. Tenorio, C. Finocchiaro, L. Gigli, M.R. Tinè, P. Mazzoleni, G. Barone, Design of alkali activated foamy binders from Sicilian volcanic precursors, Ceram. Int. 49 (2023) 38835–38846.
[22] C. Pelosi, R. Occhipinti, C. Finocchiaro, G. Lanzafame, E. Pulidori, M. Lezzerini, G. Barone, P. Mazzoleni, M.R. Tiné, Thermal and morphological investigations of alkali activated materials based on Sicilian volcanic precursors (Italy), Mater. Lett. 335 (2023) 133773.
[23] R.A. Robayo-Salazar, R.M. de Gutiérrez, Natural volcanic pozzolans as an available raw material for alkali-activated materials in the foreseeable future: a review, Constr. Build. Mater. 189 (2018) 109–118.
[24] S. Zhou, C. Lu, X. Zhu, F. Li, Upcycling of natural volcanic resources for geopolymer: comparative study on synthesis, reaction mechanism and rheological behavior, Constr. Build. Mater. 268 (2021) 121184.
[25] I. Nairn, P. Shane, J. Cole, G. Leonard, S. Self, N. Pearson, Rhyolite magma processes of the~ AD 1315 Kaharoa eruption episode, Tarawera volcano, New Zealand. J. Volcanol. Geotherm. Res. 131 (2004) 265–294.
[26] R.P. Orense, M.J. Pender. From Micro to Macro: an Investigation of the Geomechanical Behaviour of Pumice Sand, Taylor & Francis Group, London, UK, 2015. Vol. 45.
[27] M. Selby, P. Hosking, The erodibility of pumice soils of the North Island, New Zealand, J. Hydrol. (N. Z.) (1973) 32–56.
[28] O.M. Gill, R.P. Orense, Field characterisation and mapping of pumiceous deposits in central North Island, NZ, Jpn. Geotech. Soc. Spec. Publ. 6 (2019) 79–87.
[29] S. Bae, S. Park, H.-K. Lee, Role of Al in the crystal growth of alkali-activated fly ash and slag under a hydrothermal condition, Constr. Build. Mater. 239 (2020) 117842.
[30] P. Chindaprasirt, P. De Silva, K. Sagoe-Crentsil, S. Hanjitsuwan, Effect of SiO 2 and Al 2 O 3 on the setting and hardening of high calcium fly ash-based geopolymer systems, J. Mater. Sci. 47 (2012) 4876–4883.
[31] I. Garcia-Lodeiro, N. Cherfa, F. Zibouche, A. Fernandez-Jimenez, A. Palomo, The role of aluminium in alkali-activated bentonites, Mater. Struct. 48 (2015) 585–597.
[32] A. Fernández-Jiménez, A. Palomo, I. Sobrados, J. Sanz, The role played by the reactive alumina content in the alkaline activation of fly ashes, Microporous Mesoporous Mater. 91 (2006) 111–119.
[33] H. Miraki, N. Shariatmadari, P. Ghadir, S. Jahandari, Z. Tao, R. Siddique, Clayey soil stabilization using alkali-activated volcanic ash and slag, J. Rock. Mech. Geotech. Eng. 14 (2022) 576–591.
[34] P. Nasaeng, A. Wongsa, R. Cheerarot, V. Sata, P. Chindaprasirt, Strength enhancement of pumice-based geopolymer paste by incorporating recycled concrete and calcined oyster shell powders, Case Stud. Constr. Mater. 17 (2022) e01307.
[35] C. Karaaslan, E. Yener, T. Bağatur, R. Polat, Improving the durability of pumice-fly ash based geopolymer concrete with calcium aluminate cement, J. Build. Eng. 59 (2022) 105110.
[36] M. Raghav, T. Park, H.-M. Yang, S.-Y. Lee, S. Karthick, H.-S. Lee, Review of the effects of supplementary cementitious materials and chemical additives on the physical, mechanical and durability properties of hydraulic concrete, Materials 14 (2021) 7270.
[37] ASTM-E3340−22. Standard Guide for Development of Laser Diffraction Particle Size Analysis Methods for Powder Materials. 2022, 5.
[38] J. Xu, D. Zhang, Multifunctional structural supercapacitor based on graphene and geopolymer, Electrochim. Acta 224 (2017) 105–112.
[39] ASTM-C114−18. Standard Test Methods for Chemical Analysis of Hydraulic Cement. 2018, *C114-18*, 12.

[40] M.L. Nehdi, A. Yassine, Mitigating portland cement CO(2) emissions using alkali-activated materials: system dynamics model. Mater. (Basel) 13 (2020) https://doi.org/10.3390/ma13204685.
[41] J. Nyamangara, S. Munotengwa, P. Nyamugafata, G. Nyamadzawo, The effect of hydroxide solutions on the structural stability and saturated hydraulic conductivity of four tropical soils, South Afr. J. Plant Soil 24 (2007) 1–7.
[42] ASTM-C109/C109M−20. Standard Test Method for Compressive Strength of Hydraulic Cement Mortars (Using 2-in. or [50-mm] Cube Specimens). 2020.
[43] S. Pourakbar, A. Asadi, B.B. Huat, M.H. Fasihnikoutalab, Soil stabilisation with alkali-activated agro-waste, Environ. Geotech. 2 (2015) 359–370.
[44] P.K. Sarker, R. Haque, K.V. Ramgolam, Fracture behaviour of heat cured fly ash based geopolymer concrete, Mater. Des. 44 (2013) 580–586.
[45] I. García-Lodeiro, A. Fernández-Jiménez, A. Palomo, D.E. Macphee, Effect of calcium additions on N–A–S–H cementitious gels. J. Am. Ceram. Soc. 93 (2010) 1934–1940.
[46] U. Rattanasak, P. Chindaprasirt, P. Suwanvitaya, Development of high volume rice husk ash alumino silicate composites, Int. J. Miner., Metall., Mater. 17 (2010) 654–659.
[47] M.A. Hamid, N. Yaltay, M. Türkmenoğlu, Properties of pumice-fly ash based geopolymer paste, Constr. Build. Mater. 316 (2022) 125665.
[48] J.L. Provis, C.Z. Yong, P. Duxson, J.S. van Deventer, Correlating mechanical and thermal properties of sodium silicate-fly ash geopolymers, Colloids Surf. A Physicochem. Eng. Asp. 336 (2009) 57–63.
[49] Z. Zhang, X. Yao, H. Zhu, Potential application of geopolymers as protection coatings for marine concrete: II. Microstructure and anticorrosion mechanism, Appl. Clay Sci. 49 (2010) 7–12.
[50] D. Khale, R. Chaudhary, Mechanism of geopolymerization and factors influencing its development: a review, J. Mater. Sci. 42 (2007) 729–746.
[51] C. Heah, H. Kamarudin, A.M. Al Bakri, M. Bnhussain, M. Luqman, I.K. Nizar, C. Ruzaidi, Y. Liew, Study on solids-to-liquid and alkaline activator ratios on kaolin-based geopolymers, Constr. Build. Mater. 35 (2012) 912–922.
[52] Z. Zhao, F. Xiao, S. Amirkhanian, Recent applications of waste solid materials in pavement engineering, Waste Manag. 108 (2020) 78–105.
[53] H. Xu, J.S. van Deventer, The effect of alkali metals on the formation of geopolymeric gels from alkali-feldspars, Colloids Surf. A Physicochem. Eng. Asp. 216 (2003) 27–44.
[54] S. Pourakbar, B.B. Huat, A. Asadi, M.H. Fasihnikoutalab, Model study of alkali-activated waste binder for soil stabilization, Int. J. Geosynth. Ground Eng. 2 (2016) 1–12.
[55] İ.B. Topçu, T. Uygunoğlu, Influence of mineral additive type on slump-flow and yield stress of self-consolidating mortar, Sci. Res. Essays 5 (2010) 1492–1500.
[56] P. De Silva, K. Sagoe-Crenstil, V. Sirivivatnanon, Kinetics of geopolymerization: role of Al2O3 and SiO2, Cem. Concr. Res. 37 (2007) 512–518.
[57] Depasse, J. Coagulation of colloidal silica by alkaline cations: Surface dehydration or interparticle bridging? 1997, *194*, 260-262.
[58] J. Yang, D. Li, Y. Fang, Synthesis of nanoscale CaO-Al2O3-SiO2-H2O and Na2O-Al2O3-SiO2-H2O using the hydrothermal method and their characterization, Materials 10 (2017) 695.
[59] A. Hajimohammadi, T. Ngo, P. Mendis, How does aluminium foaming agent impact the geopolymer formation mechanism? Cem. Concr. Compos. 80 (2017) 277–286.
[60] Y. Yang, T.C.D. Le, I. Kudo, T.M.D. Do, K. Niihara, H. Suematsu, G. Thorogood, Pore-forming process in dehydration of metakaolin-based geopolymer. Int. J. Ceram. Eng. Sci. 3 (2021) 211–216.
[61] Z. Li, S. Zhang, Y. Zuo, W. Chen, G. Ye, Chemical deformation of metakaolin based geopolymer, Cem. Concr. Res. 120 (2019) 108–118.
[62] A. Palomo, A. Fernández-Jiménez, M. Criado, Geopolymers: same basic chemistry, different microstructures, Mater. De. ConstrucciónN. 54 (2004) 77–91.
[63] R. Occhipinti, A. Stroscio, C. Finocchiaro, M. Fugazzotto, C. Leonelli, M.J.L. Faro, B. Megna, G. Barone, P. Mazzoleni, Alkali activated materials using pumice from the Aeolian Islands (Sicily, Italy) and their potentiality for cultural heritage applications: preliminary study, Constr. Build. Mater. 259 (2020) 120391.
[64] P.N. Lemougna, A. Nzeukou, B. Aziwo, A. Tchamba, K.-t Wang, U.C. Melo, X. Cui, m. Effect of slag on the improvement of setting time and compressive strength of low reactive volcanic ash geopolymers synthetized at room temperature, Mater. Chem. Phys. 239 (2020) 122077.
[65] Z. Safari, R. Kurda, B. Al-Hadad, F. Mahmood, M. Tapan, Mechanical characteristics of pumice-based geopolymer paste, Resour., Conserv. Recycl. 162 (2020) 105055.
[66] M. Zribi, B. Samet, S. Baklouti, Effect of curing temperature on the synthesis, structure and mechanical properties of phosphate-based geopolymers, J. Non-Cryst. Solids 511 (2019) 62–67.
[67] H. Cheng, K.-L. Lin, R. Cui, C.-L. Hwang, Y.-M. Chang, T.-W. Cheng, The effects of SiO2/Na2O molar ratio on the characteristics of alkali-activated waste catalyst–metakaolin based geopolymers. Constr. Build. Mater. 95 (2015) 710–720.
[68] G.B. Singh, K.V. Subramaniam, Evaluation of sodium content and sodium hydroxide molarity on compressive strength of alkali activated low-calcium fly ash, Cem. Concr. Compos. 81 (2017) 122–132.
[69] G. Görhan, G. Kürklü, The influence of the NaOH solution on the properties of the fly ash-based geopolymer mortar cured at different temperatures, Compos. Part B Eng. 58 (2014) 371–377.
[70] E.N. Kani, A. Allahverdi, J.L. Provis, Efflorescence control in geopolymer binders based on natural pozzolan, Cem. Concr. Compos. 34 (2012) 25–33.
[71] H. Castillo, H. Collado, T. Droguett, S. Sánchez, M. Vesely, P. Garrido, S. Palma, Factors affecting the compressive strength of geopolymers: a review, Minerals 11 (2021) 1317.
[72] P. Duxson, J.L. Provis, G.C. Lukey, S.W. Mallicoat, W.M. Kriven, J.S. Van Deventer, Understanding the relationship between geopolymer composition, microstructure and mechanical properties, Colloids Surf. A: Physicochem. Eng. Asp. 269 (2005) 47–58.
[73] M. Lahoti, P. Narang, K.H. Tan, E.-H. Yang, Mix design factors and strength prediction of metakaolin-based geopolymer, Ceram. Int. 43 (2017) 11433–11441.
[74] G. Gluth, C. Lehmann, K. Rübner, H.-C. Kühne, Geopolymerization of a silica residue from waste treatment of chlorosilane production, Mater. Struct. 46 (2013) 1291–1298.
[75] W. Lee, J. Van Deventer, Use of infrared spectroscopy to study geopolymerization of heterogeneous amorphous aluminosilicates, Langmuir 19 (2003) 8726–8734.
[76] J. Madejova, P. Komadel, Baseline studies of the clay minerals society source clays: infrared methods, Clays clay Miner. 49 (2001) 410–432.
[77] S. Alonso, A. Palomo, Calorimetric study of alkaline activation of calcium hydroxide–metakaolin solid mixtures, Cem. Concr. Res. 31 (2001) 25–30.
[78] J. Van Jaarsveld, J.S. Van Deventer, G. Lukey, The effect of composition and temperature on the properties of fly ash-and kaolinite-based geopolymers, Chem. Eng. J. 89 (2002) 63–73.
[79] M. Clausi, S.C. Tarantino, L.L. Magnani, M.P. Riccardi, C. Tedeschi, M. Zema, Metakaolin as a precursor of materials for applications in Cultural Heritage: geopolymer-based mortars with ornamental stone aggregates, Appl. Clay Sci. 132 (2016) 589–599.